SM Report 94-5

Deformation Measurements at the Sub-Micron Size Scale : II. Refinements in the Algorithm for Digital Image Correlation

by

G. Vendroux and W.G. Knauss
Graduate Aeronautical Laboratories
California Institute of Technology
Pasadena, California, USA

April, 1994

Deformation Measurements at the Sub-Micron Size Scale : II. Refinements in the Algorithm for Digital Image Correlation

G. Vendroux, W.G. Knauss

Graduate Aeronautical Laboratories

California Institute of Technology

Pasadena, CA 91125

Abstract

Improvements are proposed in the application of the Digital Image Correlation method, a technique that compares digital images of a specimen surface before and after deformation to deduce its surface (2-D) displacement field and strains. These refinements, tested on translations and rigid body rotations were significant with regard to the computer efficiency and convergence properties of the method. The necessity of using the framework of large deformation theory to accurately compute large rigid body rotation is demonstrated. In addition, the formulation of the algorithm was extended so as to compute the three-dimensional surface displacement field from Scanning Tunneling Microscope topographies of a deforming specimen. The resolution of this new displacement measuring method at the nanometer scale was assessed on translation and uniaxial tensile tests and was found to be 4.8 nm for in-plane displacement components and 1.5 nm for the out-of-plane one spanning a 10×10 μm area.

Introduction

Experimental methods in solid mechanics rely heavily on surface displacement measurements. To that end, many optical methods have been developed such as optical interferometry, high resolution Moiré (Post, 1985) or CGS (Tippur *et al.*, 1991) to

name a few. In 1983, Sutton *et al.* proposed a technique by which two-dimensional correlation using white or laser speckles, may be applied to obtain the deformation of a body via comparison of digital video images of its surface in the undeformed and deformed configurations with a typical spatial resolution of $0.1\ mm$. This technique has demonstrated good flexibility and accuracy. Investigations have even been pursued to extend the method to measure three-dimensional displacement field through stereo imaging (Luo *et al.*, 1993).

As the need for smaller scale investigations related to inhomogeneous materials (fiber-matrix composites) and micromechanics issues grew, correlation based displacement measurements were performed on digital images acquired in a Scanning Electron Microscope with a spatial resolution on the order of $\approx\ 1\ \mu m$ (James *et al.*, 1990). However, in this latter case, the computations were limited to two -dimensional (in-plane) displacement field and the Fourier based correlation algorithm required strong smoothing of the results precluding the observation of eventual inhomogeneities in the displacement field at the submicron level.

In 1982, the Scanning Tunneling Microscope or STM was introduced (Binnig *et al.*, 1982). Based on the quantum tunneling effect, STMs record surface topographies with a spatial resolution ranging from an unprecedented 0.01Å to tens or even hundreds of nanometers and therefore seem particularly suited for micromechanical investigations. The though is close at hand, then, that if STM scans are compared by way of Digital Image Correlation, not only could the spatial resolution of the measurements be increased significantly and in-plane displacements and strains be measured at the nanometer scale but, in addition, since the images are surface topographies, out-of-plane displacements could be determined as well with very high accuracy.

In this paper, some modifications to the two-dimensional Digital Image Correlation algorithm as developed by the group around Sutton and McNeil are proposed to extract

the three-dimensional displacement field from STM topographs of the same specimen area before and after deformation with increased robustness and speed. In addition, some data post-processing issues are discussed which facilitate the accurate determination of rigid body rotations. Finally, experimental correlation results are presented from both standard CCD and STM images to validate the aforementioned modifications

1. The Digital Image Correlation Method

The modifications sought to the original Digital Image Correlation code (DIC) are closely tied to the inner workings of the algorithm. Therefore, the two-dimensional correlation scheme is reviewed in the following section. The three-dimensional extension to the code is then presented and its numerical implementation is discussed. Finally, some postprocessing issues related to the computation of the in-plane strains and rigid body rotation angle are addressed.

1.1 Two-dimensional Digital Image Correlation

A surface profile, as obtained by a Scanning Tunneling Microscope, is simply a discrete record of the "height" of the surface at grid points assigned to a specimen surface, the sampling interval being typically on the order of 10 nm. Let $f(x,y)$ represent the surface profile of a specimen in an undeformed state at point $G(x,y)$, and $g(\widetilde{x},\widetilde{y})$ the surface profile after deformation at point $\widetilde{G}(\widetilde{x},\widetilde{y})$. If one assumes that the profile pattern before deformation is uniquely related to the profile pattern after deformation, this suggests a correlation of these two patterns to detect the profile difference that is the object deformation. Restricting ourselves for the moment to in-plane deformation, let χ be the mapping from the undeformed to the deformed configuration, written symbolically as

$$\begin{aligned} &\chi : \mathbb{R}^2 \rightarrow \mathbb{R}^2 \\ &G \rightarrow \widetilde{G} = \chi(G) \text{ such that } g(\widetilde{x},\widetilde{y}) = f(x,y). \end{aligned} \tag{1}$$

Relation (1), expressed in terms of coordinates (x, y) and $(\widetilde{x}, \widetilde{y})$ of G and $\widetilde{G}$ respectively, can be rewritten as

$$\begin{cases} \widetilde{x} = x + u(x, y) \\ \widetilde{y} = y + v(x, y) \end{cases} \tag{2}$$

where u and v are the in-plane displacement components of G.

Let $\widetilde{G}_0$ of coordinate $(\widetilde{x}_0, \widetilde{y}_0)$ be the image of G_0 (x_0, y_0) through χ. Let S be a subset of points around G_0 and $\widetilde{S}$ be a subset around $\widetilde{G}_0$, the image of S through χ. Assuming S to be sufficiently small, equation (2) can be rewritten as

$$\forall\, \widetilde{G}(\widetilde{x}, \widetilde{y}) \in \widetilde{S}\,, \exists\, G(x, y) \in S \text{ such that}$$

$$\begin{cases} \widetilde{x} = x + u(x_0, y_0) + \dfrac{\partial u}{\partial x}|_{(x_0, y_0)}(x - x_0) + \dfrac{\partial u}{\partial y}|_{(x_0, y_0)}(y - y_0) \\ \widetilde{y} = y + v(x_0, y_0) + \dfrac{\partial v}{\partial x}|_{(x_0, y_0)}(x - x_0) + \dfrac{\partial v}{\partial y}|_{(x_0, y_0)}(y - y_0). \end{cases} \tag{3}$$

Relation (3) defines a local mapping χ_l which is the linearization of χ around G_0. Define a correlation coefficient C

$$C = \frac{\iint_S (f(G) - g(\chi_l(G)))^2\, dS}{\iint_S f^2(G)\, dS}\,, \qquad \text{Least square coefficient}$$

or

$$C = 1 - \frac{\iint_S f(G) g(\chi_l(G))\, dS}{\left[\iint_S f^2(G)\, dS \iint_S g^2(\chi_l(G))\, dS\right]^{\frac{1}{2}}}\,, \qquad \text{Cross correlation coefficient.} \tag{4}$$

It is clear that C will be zero if the coefficients of the mapping χ_l, namely $u_0 = u(x_0, y_0)$, $v_0 = v(x_0, y_0)$, $u_{0,x} = \frac{\partial u}{\partial x}|_{(x_0, y_0)}$, $v_{0,x} = \frac{\partial v}{\partial x}|_{(x_0, y_0)}$, $u_{0,y} = \frac{\partial u}{\partial y}|_{(x_0, y_0)}$ and $v_{0,y} = \frac{\partial v}{\partial y}|_{(x_0, y_0)}$, are indeed the displacements and the displacement derivatives at G_0 (Chu *et al.*, 1985, Sutton *et al.*, 1986).

The relations (4) are inappropriate when f and g are discrete sets of data; instead, the integrals in (4) are replaced by a sums over the grid points G_S contained in S,

$$\begin{cases} C = \dfrac{\sum_{G_S \in S} [f(G_S) - g(\chi_l(G_S))]^2}{\sum_{G_S \in S} f^2(G_S)} \\ \\ C = 1 - \dfrac{\sum_{G_S \in S} f(G_S) g(\chi_l(G_S))}{\left[\sum_{G_S \in S} f^2(G_S) \sum_{G_S \in S} g^2(\chi_l(G_S))\right]^{\frac{1}{2}}} \end{cases} . \tag{5}$$

The formulation presented above establishes a correspondence between the physical problem of measuring displacement to the mathematical issue of minimizing a function C with respect to six coefficients. The Digital Image Correlation algorithm can be therefore viewed as nothing but a non-linear optimization scheme, the details of which are discussed in section 1.3.b.

1.2 Three dimensional Digital Image Correlation on STM scans

The minimization of the correlation coefficient C as discussed in the preceding section should yield the in-plane displacement and displacement derivatives at a given point G_0. Since STM scans represent surface topographies, one should be able to extract the out-of-plane displacement component as well. There are two ways of obtaining this information. The first involves invoking the two dimensional correlation method, as described above. Once the displacement component (u_0, v_0) at point G_0 are known, the out-of-plane displacement w_0 can be computed as

$$w_0 = g(\tilde{x} = x_0 + u_0 , \tilde{y} = y_0 + v_0) - f(x_0 , y_0). \tag{6}$$

This scheme is very straight forward. However it is also likely to be the most error sensitive : the gradients of g may be locally large and thus a small inaccuracy in u_0 and v_0 could induce large errors in w_0.

The second approach includes directly w_0 into the computation of the correlation coefficient C and then minimizing C not only with respect to the six in-plane parameters but additionally with respect to w_0. This goal could be accomplished for any definition of a correlation coefficient; however, because of programming considerations, this technique was used here only for the least square coefficient which, in this case, can be written as

$$C = \frac{\sum_{G_S \in S} [f(G_S) - (g(\chi_l(G_S)) - w_0)]^2}{\sum_{G_S \in S} f^2(G_S)}. \tag{7}$$

In equation (7), w_0 appears now as a global offset in "height" between the two scans and assuming the dimension of subset S to be small, it approximates the out-of-plane displacement component at G_0.

Finally, it should be noted that since G_S is a grid point in the undeformed configuration, $f(G_S)$ is defined. On the other hand, $\widetilde{G} = \chi_l(G_S)$ may not be at a grid point in the deformed configuration. Consequently interpolations over the deformed field are necessary so that $g(\widetilde{G})$ is defined for any $\widetilde{G}$ in the deformed field.

1.3 Implementation of the numerical scheme

The numerical implementation of this displacement measurement technique consists of two main parts. First, an interpolation scheme was programmed to evaluate the surface height at non-grid points in the deformed topographs. Further, a second-order optimization method was devised to minimize the least square correlation coefficient with respect to the seven mapping parameters.

a. Interpolation Scheme

The Digital Image Correlation code was initially implemented with a bilinear interpolation scheme. However, the lack of C^1 continuity of this method was detrimental to the convergence properties of the overall displacement measurement technique (Bruck *et*

al., 1989), especially for rough topographic profiles. Therefore a third-degree polynomial interpolation often referred to as the bicubic spline interpolation was considered, ensuring the continuity of the topographic in-plane derivatives resulting in

$$\begin{aligned} g(\widetilde{x},\widetilde{y}) =& \alpha_{11} + \alpha_{12}\widetilde{y} + \alpha_{13}\widetilde{y}^2 + \alpha_{14}\widetilde{y}^3 \\ &+\alpha_{21}\widetilde{x} + \alpha_{22}\widetilde{x}\widetilde{y} + \alpha_{23}\widetilde{x}\widetilde{y}^2 + \alpha_{24}\widetilde{x}\widetilde{y}^3 \\ &+\alpha_{31}\widetilde{x}^2 + \alpha_{32}\widetilde{x}^2\widetilde{y} + \alpha_{33}\widetilde{x}^2\widetilde{y}^2 + \alpha_{34}\widetilde{x}^2\widetilde{y}^3 \\ &+\alpha_{41}\widetilde{x}^3 + \alpha_{42}\widetilde{x}^3\widetilde{y} + \alpha_{43}\widetilde{x}^3\widetilde{y}^2 + \alpha_{44}\widetilde{x}^3\widetilde{y}^3. \end{aligned} \tag{8}$$

The higher computational cost of this method is offset by the subsequent faster convergence rate of the optimization scheme.

b. Optimization Scheme

The most important feature of the correlation scheme is the minimization of C in equation (7) with respect to the mapping parameters of χ_l, namely u_0, v_0, $u_{0,x}$, $v_{0,y}$, $u_{0,y}$, $v_{0,x}$ and the out-of-plane component w_0. Let these seven quantities define a seven-dimensional space D such that

$$D = \left\{ P \in \mathbb{R}^7 \mid P(u, v, u_x, v_y, u_y, v_x, w) \right\}. \tag{9}$$

Thus, if P is the unknown vector, the mapping χ_l can be considered to be a function of P and, through χ_l in (7), $C = C(P)$, that is

$$C(P) = \frac{\sum_{G_S \in S} [f(G_S) - \widetilde{g}(G_S, P)]^2}{\sum_{G_p \in S} f^2(G_p)} \tag{10}$$

where

$$\widetilde{g}(G_S, P) = g(\chi_l(G_S)) - w. \tag{11}$$

Let P_0 be a vector in D and let P be the vector solution of the minimization problem. Writing $C(P)$ as a truncated Taylor series around P_0 leads to

$$C(P) = C(P_0) + \nabla C(P_0)^T (P - P_0) + \frac{1}{2}(P - P_0)^T \nabla\nabla C(P_0)(P - P_0)\,. \tag{12}$$

Since P defines a minimum, $\nabla C(P) = 0$. Consequently, taking the gradient of (12) yields

$$\nabla\nabla C(P_0)(P - P_0) = -\nabla C(P_0). \tag{13}$$

Solving for P iteratively from equation (13) will converge to the solution of the minimization problem. This scheme, called the Newton-Raphson optimization method (Bruck *et al.*,1989), may be computer intensive since it requires the knowledge of $\nabla\nabla C(P)$, the Hessian matrix of C at P, defined as

$$\nabla\nabla C(P) = \left(\frac{\partial^2 C}{\partial P_i \partial P_j}\right)_{i=1,7;j=1,7}. \tag{14}$$

However, we note that, if C is chosen according to (7), it may then only be necessary to compute the first derivatives of C with respect to P, *i.e.* the components of ∇C,

$$\nabla(C) = \left(\frac{\partial C}{\partial P_i}\right)_{i=1,7}. \tag{15}$$

To show this, we find from (10)

$$\frac{\partial C}{\partial P_i} = -\frac{2}{\sum_{G_S \in S} f^2(G_S)} \sum_{G_S \in S} [f(G_S) - \tilde{g}(G_S, P)] \frac{\partial \tilde{g}(G_S, P)}{\partial P_i}, \tag{16}$$

and upon taking another derivative, Hessian matrix terms are obtained as

$$\begin{aligned} \frac{\partial^2 C}{\partial P_i \partial P_j} = & -\frac{2}{\sum_{G_S \in S} f^2(G_S)} \sum_{G_S \in S} [f(G_S) - \tilde{g}(G_S, P)] \frac{\partial^2 \tilde{g}(G_S, P)}{\partial P_i \partial P_j} \\ & + \frac{2}{\sum_{G_S \in S} f^2(G_S)} \sum_{G_S \in S} \frac{\partial \tilde{g}(G_S, P)}{\partial P_i} \frac{\partial \tilde{g}(G_S, P)}{\partial P_j}. \end{aligned} \tag{17}$$

Equation (17) gives an exact formulation of the Hessian matrix of C at P. However (17) can be approximated when P is close to the exact solution (Jayakumar, 1987). In that case

$$\tilde{g}(G_S, P) \approx f(G_S) \tag{18}$$

and therefore

$$\frac{\partial^2 C}{\partial P_i \partial P_j} \approx \frac{2}{\sum_{G_S \in S} f^2(G_S)} \sum_{G_S \in S} \frac{\partial \tilde{g}(G_S, P)}{\partial P_i} \frac{\partial \tilde{g}(G_S, P)}{\partial P_j}. \tag{19}$$

This approximation in the calculation of the Hessian matrix makes the method easy to implement since equation (19) involves terms such as $\frac{\partial \tilde{g}(G_S,P)}{\partial P_i}$ which are now very simple to obtain.Through the bicubic spline interpolation, $\tilde{g}(G_S,P)$ can be written as

$$\begin{aligned}\tilde{g}(G_S,P) =& g(\tilde{x},\tilde{y}) - w \\ =& \alpha_{11} + \alpha_{12}\tilde{y} + \alpha_{13}\tilde{y}^2 + \alpha_{14}\tilde{y}^3 \\ &+\alpha_{21}\tilde{x} + \alpha_{22}\tilde{x}\tilde{y} + \alpha_{23}\tilde{x}\tilde{y}^2 + \alpha_{24}\tilde{x}\tilde{y}^3 \\ &+\alpha_{31}\tilde{x}^2 + \alpha_{32}\tilde{x}^2\tilde{y} + \alpha_{33}\tilde{x}^2\tilde{y}^2 + \alpha_{34}\tilde{x}^2\tilde{y}^3 \\ &+\alpha_{41}\tilde{x}^3 + \alpha_{42}\tilde{x}^3\tilde{y} + \alpha_{43}\tilde{x}^3\tilde{y}^2 + \alpha_{44}\tilde{x}^3\tilde{y}^3 - w.\end{aligned} \tag{20}$$

The relation between $\tilde{x}$, $\tilde{y}$, x, and y is then

$$\begin{cases} \tilde{x} = x_0 + \overline{x} + P_1 + P_3\overline{x} + P_5\overline{y} \\ \tilde{y} = y_0 + \overline{y} + P_2 + P_4\overline{y} + P_6\overline{x}, \end{cases} \tag{21}$$

with

$$\begin{cases} \overline{x} = x - x_0 \\ \overline{y} = y - y_0, \end{cases} \tag{22}$$

so that, finally, the various terms $\frac{\partial \tilde{g}(G_S,P)}{\partial P_i}$ may be calculated as

$$\left.\begin{aligned}
\frac{\partial\tilde{g}(G_S,P)}{\partial P_1} &= \frac{\partial\tilde{g}(G_S,P)}{\partial\tilde{x}}\frac{\partial\tilde{x}}{\partial P_1} + \frac{\partial\tilde{g}(G_S,P)}{\partial\tilde{y}}\frac{\partial\tilde{y}}{\partial P_1} = \frac{\partial\tilde{g}(G_S,P)}{\partial\tilde{x}} \\
\frac{\partial\tilde{g}(G_S,P)}{\partial P_2} &= \frac{\partial\tilde{g}(G_S,P)}{\partial\tilde{x}}\frac{\partial\tilde{x}}{\partial P_2} + \frac{\partial\tilde{g}(G_S,P)}{\partial\tilde{y}}\frac{\partial\tilde{y}}{\partial P_2} = \frac{\partial\tilde{g}(G_S,P)}{\partial\tilde{y}} \\
\frac{\partial\tilde{g}(G_S,P)}{\partial P_3} &= \frac{\partial\tilde{g}(G_S,P)}{\partial\tilde{x}}\frac{\partial\tilde{x}}{\partial P_3} + \frac{\partial\tilde{g}(G_S,P)}{\partial\tilde{y}}\frac{\partial\tilde{y}}{\partial P_3} = \overline{x}\frac{\partial\tilde{g}(G_S,P)}{\partial\tilde{x}} \\
\frac{\partial\tilde{g}(G_S,P)}{\partial P_4} &= \frac{\partial\tilde{g}(G_S,P)}{\partial\tilde{x}}\frac{\partial\tilde{x}}{\partial P_4} + \frac{\partial\tilde{g}(G_S,P)}{\partial\tilde{y}}\frac{\partial\tilde{y}}{\partial P_4} = \overline{y}\frac{\partial\tilde{g}(G_S,P)}{\partial\tilde{y}} \\
\frac{\partial\tilde{g}(G_S,P)}{\partial P_5} &= \frac{\partial\tilde{g}(G_S,P)}{\partial\tilde{x}}\frac{\partial\tilde{x}}{\partial P_5} + \frac{\partial\tilde{g}(G_S,P)}{\partial\tilde{y}}\frac{\partial\tilde{y}}{\partial P_5} = \overline{y}\frac{\partial\tilde{g}(G_S,P)}{\partial\tilde{x}} \\
\frac{\partial\tilde{g}(G_S,P)}{\partial P_6} &= \frac{\partial\tilde{g}(G_S,P)}{\partial\tilde{x}}\frac{\partial\tilde{x}}{\partial P_6} + \frac{\partial\tilde{g}(G_S,P)}{\partial\tilde{y}}\frac{\partial\tilde{y}}{\partial P_6} = \overline{x}\frac{\partial\tilde{g}(G_S,P)}{\partial\tilde{y}} \\
\frac{\partial\tilde{g}(G_S,P)}{\partial P_7} &= \frac{\partial\tilde{g}(G_S,P)}{\partial\tilde{x}}\frac{\partial\tilde{x}}{\partial P_7} + \frac{\partial\tilde{g}(G_S,P)}{\partial\tilde{y}}\frac{\partial\tilde{y}}{\partial P_7} = 1
\end{aligned}\right\}. \tag{23}$$

Derivatives of $\tilde{g}(G_S,P)$ with respect to $\tilde{x}$ or $\tilde{y}$ are easily computed from (20).

This minimization method depends on the starting point P_0. Before executing this calculation, a coarse optimization scheme determines therefore an initial guess : the displacement derivatives and out-of-plane displacement are set to zero and all possible integer values of u_0, v_0 within a given range are tried. The set $(u_0, v_0, 0, 0, 0, 0, 0)$ that produces the lowest correlation coefficient is then used as the starting guess for the optimization procedure.

1.4 Postprocessing

Comparing two images with Digital Image Correlation yields seven variables at preselected pixel locations in the reference image, namely u, v, w, u_x, u_y, v_x, v_y. These parameters define locally the mapping that brings the undeformed image to the deformed one. It is then possible to extract the local in-plane strains at each computational point from the displacement gradients which one determines.

Earlier work on the method (Sutton *et al.*, 1986) has employed the framework of small deformation theory to compute in-plane strains and the local rigid body rotation angle θ

$$\begin{cases} \epsilon = \frac{1}{2}(\nabla \mathbf{u} + \nabla \mathbf{u}^T) \\ \theta = \frac{1}{2}(\frac{\partial v}{\partial x} - \frac{\partial u}{\partial y}). \end{cases} \tag{24}$$

However preliminary tests of this code showed that when two images were compared, which differed only by a rigid body rotation of angle θ, this angle could only be deduced accurately for $\theta \leq 10°$; in addition and more importantly, erroneous rotation-induced "straining" was observed. This inconsistency is implicit in the small deformation theory itself. To show this, let us assume that the deformed image is the result of a rigid body rotation of amount θ of the reference image; a point P of coordinate (x, y) in the undeformed configuration is then mapped to $\widetilde{P}$ ($\widetilde{x}, \widetilde{y}$) in the deformed configuration by

$$\begin{cases} \widetilde{x} = x\, cos\theta - y\, sin\theta \\ \widetilde{y} = x\, sin\theta + y\, cos\theta. \end{cases} \tag{25}$$

Consequently, the resulting displacement components u and v are :

$$\begin{cases} u = \tilde{x} - x = x\,(\,cos\theta - 1\,) - y\,sin\theta \\ v = \tilde{y} - y = x\,sin\theta + y\,(\,cos\theta - 1\,). \end{cases} \tag{26}$$

From u and v, the components of the strain tensor ϵ_{xx}, ϵ_{yy}, ϵ_{xy} as well as the apparent rigid body rotation angle θ' can be computed as

$$\begin{aligned} \epsilon_{xx} &= \frac{\partial u}{\partial x} = cos\theta - 1 \\ \epsilon_{yy} &= \frac{\partial v}{\partial y} = cos\theta - 1 \\ \epsilon_{xy} &= \frac{1}{2}(\,\frac{\partial u}{\partial y} + \frac{\partial v}{\partial x}\,) = 0 \\ \theta' &= \frac{1}{2}(\,\frac{\partial v}{\partial x} - \frac{\partial u}{\partial y}\,) = sin\theta. \end{aligned} \tag{27}$$

If "θ is small enough" (small deformation theory), equation (27) becomes

$$\begin{aligned} \epsilon_{xx} &= O(\,\theta^2\,) \\ \epsilon_{yy} &= O(\,\theta^2\,) \\ \epsilon_{xy} &= 0 \\ \theta' &= \theta + O(\,\theta^3\,). \end{aligned} \tag{28}$$

Thus, as long as $O(\,\theta^2\,)$ is below the resolution of the Digital Image Correlation code, processing its output in the small deformation theory framework will yield an accurate estimate for the local strain tensor components and rigid body rotation angle. It was found, however, that the resolution in strain from correlation data can be as low as 2×10^{-4} (Bruck *et al.*, 1989) which means that rigid body rotation of the amount of 1° will induce an apparent detectable (small deformation) strain. In other words, the "sufficiently small θ" statement translates for our purposes to "$\theta \ll 1°$ " to rightfully use the small deformation theory for processing the data.

It is experimentally very difficult to guarantee that deforming a specimen will not induce a rigid body rotation of more than 1° and it becomes thus mandatory to draw on the large deformation theory. Accordingly, the in-plane deformation tensor $\mathbf{F}$, the Right Cauchy-Green tensor $\mathbf{C}$ and the Lagrangian strain tensor γ are evaluated at every computational point from u_x, u_y, v_x and v_y by

$$\mathbf{F} = (\mathbf{1} + \nabla\mathbf{u}), \quad \mathbf{C} = \mathbf{F}^T\mathbf{F}, \quad \gamma = \frac{1}{2}(\mathbf{C} - \mathbf{1}) \tag{29}$$

The local rigid body deformation part of the deformation process $\mathbf{Q}$ may then be computed through the Polar Decomposition Theorem,

$$\mathbf{Q} = \mathbf{F}(\sqrt{\mathbf{C}})^{-1}. \tag{30}$$

In component form, $\mathbf{Q}$ can be written as

$$Q = \begin{pmatrix} cos\theta & -sin\theta \\ sin\theta & cos\theta \end{pmatrix} \tag{31}$$

and hence θ can be computed. An error analysis of this formulation reveals that

$$\begin{cases} \text{Error in } \gamma \approx \text{Error in } \dfrac{\partial u}{\partial x}, \dfrac{\partial u}{\partial y}, \dfrac{\partial v}{\partial x}, \dfrac{\partial v}{\partial y} \\ \text{Error in } tan(\theta) \approx \text{Error in } \dfrac{\partial u}{\partial x}, \dfrac{\partial u}{\partial y}, \dfrac{\partial v}{\partial x}, \dfrac{\partial v}{\partial y}. \end{cases} \tag{32}$$

Therefore, if the uncertainty in the in-plane displacement derivatives is 10^{-3}, it will result in an error of 0.1% in strains whereas the error in the rigid body rotation angle θ will be at most 10^{-3} radians or 5.7×10^{-2} °. We thus expect the determination of θ to be more accurate than that of strains.

There is more to the accurate computation of θ than merely extracting another deformation parameter from the comparison of two images; it is also essential to the proper and understandable representation of the displacement field: If the mapping between the undeformed and deformed image is a combination of a deformation process superposed

on some rigid body rotation, the in-plane displacement component will reflect both. It follows that, if the deformation induced displacements are small compared to the field under observation, the displacements induced by the rigid rotation will cloud the data. It is therefore extremely important to accurately extract any rotation $\mathbf{Q}$ (and to correct, if necessary, the data accordingly by ascribing the measured displacement to a rotation $\mathbf{Q}^{-1}$). To this end, the global rigid body rotation of a given deformation field is estimated by taking the average of the local rigid body rotation angle at every pixel location where DIC computations are carried out.

2. Experimental Code Validation

In order to explore the computational efficiency of the method, four different Digital Image Correlation codes (DIC) were written around the same skeleton scheme. The first code, referred to as the Exact Least Square DIC, implements the two dimensional correlation method with the exact Hessian matrix calculation for the Least Square Correlation coefficient (eq. (17)). The second, referred to as the Approximate DIC, is also a two dimensional scheme but uses the approximate Hessian matrix formulation for the Least Square Correlation coefficient (eq. (19)). The third code is the now well accepted DIC based on the Cross-Correlation coefficient developed by Sutton *et al.* (Sutton *et al.*, 1983, Bruck *et al.*, 1989). Finally, the fourth program, referred to as three dimensional DIC, is the extension of the Approximate DIC scheme to three dimensions (eq. (7)), that is, it involves, besides the in-plane displacement and displacement derivatives the out-of-plane displacement component as well.

Four sets of experiments were carried out to evaluate the four correlation programs and to assess their performance. First, translation tests were performed on speckle patterns (not STM data) using a CCD camera-frame grabber combination. The subsequent images were compared through each of the four DIC schemes to check their accuracy and resolution. Second, rotation tests were performed on the same white speckle pattern

to assess the validity of the data processing scheme presented in section 1.4. Finally translation and uniaxial tensile tests were carried out with a specifically designed Scanning Tunneling Microscope (Vendroux and Knauss, 1994a). The resulting topographs were compared by way of the three dimensional DIC so as to evaluate the STM-DIC scheme as a full displacement field measurement method at the nanometer scale. The following presents the results of these experiments.

2.1 Translation Tests on Speckle Patterns

These experiments were performed on PMMA specimens which surfaces were first coated with a layer of white paint and then splattered with black paint so as to create a speckle pattern as shown in Figure 1. The specimens were mounted on a translation stage driven by a NRC actuator (model 360-30) with a resolution of 0.1 μm and its surface was imaged by an 8-bit CCD camera possessing a 640 $\times$ 480 square pixel viewing field. The magnification of the optical set-up was determined by measuring the distance between two marks on the specimen surface by way of a microscope ($\times$100) and by determining the location of the corresponding pixels in the digital images. This calibration yielded a pixel size of 0.06647 mm $\pm$0.3%.[a] Digital images of the specimen surface were acquired for various amounts of translation through a frame grabber board in a 486-50 MHz PC. Each image was then compared to the first image of the translation sequence by way of the four DIC codes on a Sun station LX. The displacement field was computed at 121 points which positions (x_i, y_j) were defined in the reference image as

$$\begin{cases} x_i = 270 + 10(i-1) \;\; i = 1,11 \\ y_j = 190 + 10(j-1) \;\; j = 1,11. \end{cases} \tag{33}$$

[a] The error bar on the pixel size was estimated by evaluating the error associated with both the distance measurement under the microscope, namely $\pm$0.01 mm, and determination of the corresponding pixel locations, *i.e.* $\pm$1 *pixel*.

Each computation was carried out with a subset size of 41×41 *pixel* centered at every computational point and involved the determination of the in-plane displacement component u and v, the in-plane strains γ_{xx}, γ_{yy}, γ_{xy} and the rigid body rotation angle θ. The codes also provided the average and standard deviation of all these quantities at the 121 points.

Figure 2 presents a comparison between the prescribed displacement and the result of the Exact Least Square DIC. A straight line is least square fitted to the experimental data and its equation is found to be

$$\text{Meas. Translation (pixel)} = 0.9984\ \text{Prescr. Translation (pixel)} - 9.94 \times 10^{-3} \quad (34)$$

The average error associated with the Exact DIC computations amounts to 0.17% which is well within the calibration error of the pixel size (0.3%). While these results validate the DIC algorithm, one needs to assess the error pointwise to compare the performance of the four codes. Table 1 presents the standard deviation of the total measured in-plane displacement $s(\sqrt{u^2+v^2})$ as well as the standard deviation of the three in-plane strains $s(\gamma_{xx})$, $s(\gamma_{yy})$, $s(\gamma_{xy})$, the average rigid body rotation angle $\overline{\theta}$, its standard deviation $s(\theta)$ and finally the average total computational time for the four DIC schemes.

We first note that all four codes render very comparable performance. The size of the measured translation $\sqrt{u^2+v^2}$ differs maximally by only 2×10^{-3} pixel at each computational points for these DIC schemes. The standard deviation of the displacement computation over the field reveals how uniform the translation is: It quantifies the error associated with DIC methods in determining in-plane displacement information from the comparison of two digital images before and after deformation. Therefore we can assert that, for any of the four DIC codes, the resolution in the in-plane displacement component is statistically equal to the standard deviation of the translation field as presented in Table 1, that is, conservatively, 10^{-2} *pixel*. This figure compares well with what has been achieved in previous work (Bruck *et al.*, 1989).

Following the same rationale to analyze the in-plane strain results, one estimates the strain resolution to be 8×10^{-4} $pixel/pixel$. This number is again consistent with the results from other correlation codes. However, the error is large enough to preclude the use of the computed strains to accurately characterize the deformation field pointwise. Because of equation (32), the error on the rigid body rotation is nevertheless very reasonable at 3.26×10^{-2} °.

While the results in Table 1 suggest that the four DIC schemes perform numerically similarly, the efficiency of each of the code, measured by the average computation time are measurably different. Focussing first on the three two-dimensional schemes, the approximate least square formulation runs 12% faster than the exact least square one and 25% faster than the cross correlation's for the same resolution. The computational speed is scaled by the complexity of the Hessian matrix calculation at each iteration and therefore the simplest code, *i.e.* the approximate least square scheme outperforms the other two. The three-dimensional DIC code adds one more degree of freedom to the problem (the out-of-plane displacement component) and is thereby slower than the approximate scheme but still faster than the exact ones.

A further argument is made in favor of the approximate least square DIC formulation if one examines the convergence properties of the four codes. Such characteristics were obtained by executing the optimization routine of each of the schemes on two images translated relative to each other by a known amount; but, rather than using a coarse search routine to obtain a first approximation of the translation, the algorithm was started at a user defined guess of the in-plane displacement component u and v, the in-plane displacement derivatives being set systematically at zero. Let u_0 and v_0 be the actual translation along the X and Y axes between the two images. Let u and v be the guess entered in the optimization routine. One can assess the adequacy of the guess by considering the

quantity

$$r = \sqrt{(u-u_0)^2+(v-v_0)^2} \tag{35}$$

The largest value of r for which the optimization scheme, starting at (u,v), converges systematically to (u_0,v_0) is called the "radius of convergence", denoted by R, which characterizes the robustness of the different algorithms. Obviously the value of R is dependent on the two images involved in the correlation as well as on the specific location at which they are compared; but R was found to be consistent within one pixel from point to point and from one pair of images to another, therefore offering a reliable measure of the convergence properties for a given DIC code. Table 2 presents the average values of the radius of convergence R for the four different DIC codes.

These results indicates that, for the same final computational result, the robustness of the DIC schemes based on the approximate least square formulation is much better than that for both exact formulations. A tentative explanation for this result lies in the fact that the two exact schemes require the computation of the second derivatives of the image intensity with respect to the six parameters of the deformation mapping (see equation (17)). This calculation seems to incur more error than it is supposed to correct. The approximate formulation, involving only the first derivatives of the image intensity appears to yield a more accurate Hessian matrix and therefore the convergence properties are better.

From the results of the translation experiments, it appears that the approximate formulation of the Hessian matrix based on the least square correlation coefficient provides the same resolution as any other schemes but at higher speed and with greater robustness. The three-dimensional DIC, also based on the same approximation, exhibits similar performance as its two-dimensional counterpart with a slightly reduced computational efficiency due to the addition of one more degree of freedom to its optimization routine. Therefore, in the rest of this work, every displacement field measurement is performed

by way of the three dimensional approximate DIC code.

2.2 Rotation Tests on White Speckle Patterns

While the translation test discussed above validated and selected an efficient and robust DIC code (approximate evaluation of the Hessian matrix for a least square correlation coefficient) the following rotation experiments were performed to confirm the necessity of using the large deformation theory framework to accurately characterize deformation fields.

The rotation tests were performed on the same speckle pattern as used in the translation tests. The specimen was mounted on a manual rotation stage with a resolution capability of 8.4×10^{-2} °. Digital images of the specimen surface were acquired for various amounts of rotation and each image was then compared to the first image of the sequence by way of the three dimensional approximate least square DIC algorithm. The computations were carried out at the same 121 points as in the translation experiments with a subset size set at 41×41 *pixel*.[b]

Figure 3 presents a comparison between the prescribed rotation and the average rotation over the field, as computed by way of DIC. A straight line, least square fitted to the experimental data, is represented by

$$\text{Meas. rotation (degree)} = 0.99942\ \text{Prescr. rotation (degree)} - 8.9 \times 10^{-3}\ ^\circ \qquad (36)$$

The average error in the correlation calculations, quantified by the deviation of the leading coefficient of the straight line from unity, therefore amounts to less than 10^{-3} ° which is about 1/10 of the uncertainty associated with the use of the rotation stage. As for the translation test, the pointwise error in the measurements of the rigid body rotation can be evaluated by the average standard deviation of the angle computed for all the images

[b] Note that for the rotation tests, no pixel calibration is necessary.

considered. That error was found to be $\pm 4.1 \times 10^{-2}$ ° which therefore validates the use of the large deformation theory formulation to measure the rigid body rotation angle consistently over the computational field.

The strains associated with the various rotations are supposed to be identically zero. However, even within the large deformation theory framework, we observed computed strain amplitudes amounting to 0.01%, 0.07% and 3% for a rigid body rotation angle of 1°, 10° and 90° respectively.For comparison, we note that small deformation theory yields, for the same angles, strains of 0.015%, 1.5% and 100% respectively.

Three techniques have been proposed to increase the DIC resolution in strains (Sutton *et al.*, 1988). The first one consists of acquiring not one but several (20) digital images of the specimen surface in the same deformation state and of averaging their intensity, thus reducing the digitization errors associated with CCD cameras. The second is based on increasing the subset size over which the correlation is performed at a given computational point. The last and most efficient of these methods involves the smoothing of the computed displacement field and its subsequent differentiation to calculate the strains. With this indirect technique the strain resolution can be improved to 2×10^{-4}. If such is the resolution desired, one needs to be aware that, according to equation (27), the small deformation theory formulation will translate a 1° into an "apparent" uniaxial strain of 1.5×10^{-4}. It is therefore imperative that the large deformation theory be considered not only to determine the rigid body rotation accurately but also to compute a rotation-independent Lagrangian strain tensor.

3. Displacement Measurements using Scanning Tunneling Microscopy

In parallel to the implementation of the three dimensional DIC, a Scanning Tunneling Microscope (STM) was designed and constructed which would accommodate *in-situ* deformation of macroscopic specimens (Vendroux ank Knauss, 1994a). Scanning Tunneling Microscopy is based on the local tunneling of electron between the conductive

surface of a specimen and a very sharp conductive tip (Binnig *et al.*, 1982). The resulting tunneling current, measured at scan grid points over the specimen allow for the surface topography to be determined with very high resolution both in the plane of the specimen surface and perpendicular to it. It is beyond the scope of this paper to detail the working principle or particularities of our custom STM except to state that a typical scan acquired by this microscope has the following characteristics:

Pixel size (spatial resolution) = 30.45 nm

Scan size = 300 × 300 $pixel$ or 9135 × 9135 μm

bit per pixel = 16

Least Significant Bit (LSB) in out-of-plane measurement = 8.26×10^{-3} nm

Out-of-plane resolution[c] = 6.6×10^{-2} nm

Conceptually, an STM topograph is similar to a digital image acquired by a CCD camera: rather than characterizing the light intensity reflected from the surface of a specimen at a given pixel location, it reports the relative height of the surface at that point. Two sets of tests were performed under the STM, translation tests and uniaxial tensile tests. The following sections presents the results of these experiments.

3.1 Translation Tests

The three dimensional correlation algorithm was found in section 2.1 to have a 10^{-2} $pixel$ resolution in the in-plane displacement components measurements on CCD acquired images. Assuming that the code would perform similarly on STM topographs, one would expect a resolution in the same quantities of 0.3 nm. It is very difficult to translate a macroscopic specimen with that amount of accuracy and, therefore, rather than actually determining the translation vector between two STM profiles, attention focused on

---

[c] The difference between the LSB in out-of-plane measurement ant the out-of-plane resolution is explained by the amount of noise in the piezoelectric/mechanical system (± 4 LSB).

assessing how uniformly the translation under the STM was recorded. To that end pairs of topographs of the same specimen surface area were acquired and compared by way of the three dimensional DIC and the standard deviations of the three displacement components were computed, thereby evaluating the pointwise error in the full displacement field measurements.

These "translation" tests were performed on PVC specimens that were lightly polished and coated with a 40 nm thick gold-palladium layer (to ensure the conductivity of the specimens surfaces). A typical topography of such a surface is presented in Figure 4, each gray level in the image representing a given elevation of the surface. Pairs of profiles of the same specimen area were acquired and compared by way of three dimensional DIC at 121 points which location (x_i, y_j) in the reference image were defined as

$$\begin{cases} x_i = 100 + 10(i-1) \;\; i = 1,11 \\ y_j = 100 + 10(j-1) \;\; j = 1,11. \end{cases} \tag{37}$$

Finally, calculations were carried out with a subset size of 41 × 41 $pixel$ and the three displacement component u, v and w were computed along with their standard deviations $s(u)$, $s(v)$ and $s(w)$. Table 3 presents the average of these standard deviations $\overline{s(u)}$, $\overline{s(v)}$ and $\overline{s(w)}$ over the number of tests that were performed.

Converting these results into nanometer units and considering the standard deviation of the displacement component over the field as a statistical error associated with their measurements, we can assess the resolution of the STM-DIC scheme as

Resolution in in-plane displacement component = 4.8 nm

Resolution in out-of-plane displacement component = 1.5 nm.

The value of the standard deviation for the in-plane displacement components presented in Table 3 are significantly higher than those recorded for the translation experiments on CCD images. Two factors contribute to that difference. First, the features contained in a speckle pattern are widely different from those in an STM topography: while speckle

pattern images contain large amounts of medium to high spatial frequencies, STM profiles are much smoother. DIC requires high frequency information within the correlation subset to fine-tune its calculation; the lower the high frequency content, the lower the consistency of the measurements and therefore the higher the standard deviation. The second cause for higher standard deviation in DIC computation on STM scans lies in the functioning of the microscope itself. In such an apparatus, a specimen topograph is obtained by scanning the surface with the tunneling probe by way of a piezoceramic actuator. Non-linearities in the piezoceramic (hysteresis, creep) and/or electrical noise in the system affect the accuracy with which the scanning probe is positioned over the roster points. Such uncertainty is reflected in subsequent DIC computations by a higher standard deviation in the measured displacement components.[d]

3.2 Uniaxial Tensile Tests

To further validate the STM-DIC combination as a three dimensional displacement field measurement method, uniaxial tensile tests were performed. Thin strips of PVC, 28 *mm* long and 1/32" thick were lightly polished, coated with 40 *nm* gold-palladium and positioned in a load frame specially designed to fit under the microscope (Vendroux, 1994c). The specimens were then pulled *in-situ*, while the tip was within tunneling range and scans of the same specimen area were acquired at different load levels. These topographies were then compared by way of Digital Image Correlation and three dimensional displacement fields were obtained corresponding to given load increments. Figure 5 presents an example of such a test sequence. In that specific case, the loading direction was 9.5° off the Y (observation) axis[e] and the reference scan was acquired at the highest

---

[d] Actually the three dimensional DIC results on STM scans have exposed the limitations of the classical scanning devices in STMs and based on this knowledge a new scanning head design is currently being developed to increase the consistency of STM measurements.

[e] The current STM design does not allow for any in-plane rotation adjustment of the STM with respect to the specimen.

load level of the experiment (unloading test), thus yielding an apparent compression. The uniaxial strain along the loading direction can easily be evaluated from such data and Figure 6 presents a comparison between strains measured with the STM and strains recorded by way of a strain gauge attached to the specimen surface.

The agreement between the macroscopic and microscopic strain is good, especially at low strain levels ($< 0.01\ m/m$). For higher strains, the STM results tend to underestimate the strain gauge readings. It is believed that this inconsistency is related to the deformation mechanisms of PVC as explained in (Vendroux and Knauss, 1994b).

Conclusion

Digital Image Correlation is a technique that compares digital images of a specimen before and after deformation to deduce the two dimensional displacement field and two dimensional strain field of its surface. The core of the method lies in the optimization of a correlation coefficient between the two images over six parameters characterizing the in-plane deformation, namely the in-plane displacement components u and v and the in-plane displacement derivatives du/dx, du/dy, dv/dx and dv/dy. The original code (Sutton *et al.*, 1983, Bruck *et al.*, 1989) was developed based on the computation of a cross-correlation coefficient minimized by a Newton-Raphson numerical scheme and a small deformation theory framework to calculate the strains and rigid body rotation angle from the in-plane displacement derivatives.

The present work proposes an alternate formulation of the Digital Image Correlation algorithm as well as of its data processing. First, it was found that, if the image comparison is performed by way of a least square coefficient, the Newton-Raphson scheme can be greatly simplified. The testing of this modified scheme on experimental data showed it was not only 25% faster than the original technique for the same resolution in displacement measurement, but also that the convergence robustness of the code was significantly improved. Second, implementing a large deformation theory formulation to compute

the strains and rigid body rotation angle from the in-plane displacement components and derivatives was shown to provide a significantly improved method to characterize the deformation field in that large rigid body rotation angles can be accurately computed (up to 90°). In addition, such a processing reduces the coupling between rigid body rotation and strains measurably. This feature is particularly important when one investigates deforming systems for which the rigid body rotation is expected to be locally larger than 1°, as, for example, in crack problems since in these cases the small deformation theory formulation will yield "apparent" uniaxial strains which are likely to be larger than the claimed resolution of the method.

An extension of the alternate correlation algorithm is also presented to compute three dimensional displacement field from topographic profile of a deforming specimen surface obtained by way of Scanning Tunneling Microscope (STM). This further modification in the correlation scheme was validated by *in-situ* translation and uniaxial tensile tests performed under a specifically designed STM and the resolution in displacement field measurement was found to be 4.8 nm for in-plane displacement components and 1.5 nm for out-of-plane's over a 10×10 μm area.

The three dimensional correlation scheme is readily applicable to topographies obtained by means other than Probe Microscopy (STM, AFM,...). In particular Confocal Microscopy seems particularly suited for such an application since it also yield surface profile data of a specimen but at a scale larger than that of STMs, namely from about a few millimeters to 60 μm. Therefore correlation based algorithms could provide a universal method to measure three dimensional surface displacement field, by way of stereo imaging for large scales, by way of Confocal Microscopy for intermediate dimension and finally by way of Probe Microscopy for scale ranging from tens of microns to atomistic dimensions.

Acknowledgments

This work has been supported by the National Science Foundation under grant MSS 9109973 for the hardware component of the STM. Also additional assistance through the Office of Naval Research (grant N00014-91-5-1427) and the Albert and Marguerite Ramond fellowship is gratefully acknowledged. In addition, the authors wish to thank H. Lu, graduate student, for his help in providing some of the experimental data.

References

Binnig G., Rohrer H., Gerber Ch., Weibel E., 1982, "Tunneling through a controllable vacuum gap", Applied Physics Letters, Vol. 40, pp 178-180.

Bruck H.A., McNeil S.R., Sutton M.A. and Peters W.H., 1989, "Digital Image Correlation using Newton-Raphson method of partial differential correction", Experimental Mechanics, **29(3)**, pp.261-267.

Chu T.C., Ranson W.F., Sutton M.A. and Peters W.H., 1985, "Applications of Digital Image Correlation techniques to experimental mechanics", Experimental Mechanics, **25(3)**, pp.232-244.

James M.R., Morris W.L. and Cox B.N, 1990, "A high accuracy automated strain-field mapper", Experimental Mechanics, **30(1)**, pp.60-67.

Jayakumar P., 1987, "Modeling and Identification in structural dynamics", Ph.D thesis, Report EERL 87-01 CALTECH, pp.146-149.

Luo P.F., Chao Y.J., Sutton M.A. and Peters W.H., 1993, "Accurate measurement of 3-dimensional deformations in deformable and rigid bodies using computer vision", Experimental Mechanics, **33(2)**, pp. 123-132.

Post D., 1985, "Moiré interferometry for deformation and strain studies", Optical Engineering, **24**, pp.663-667.

Sutton M.A., Wolters W.J., Peters W.H., Ranson W.F. and McNeil S.R., 1983, "Determination of Displacements using and improved Digital Correlation Method", Image Vision Computing, **1(3)**, pp.133-139.

Sutton M.A., Cheng M., Peters W.H., Chao Y.J. and McNeil S.R., 1986, "Application of an optimized Digital Image Correlation method to planar deformation analysis", Image Vision Computing, **4(3)**, pp.143-150.

Sutton M.A., McNeil S.R., Jang J. and Babai M., 1988, "The effect of subpixel image restauration on Digital Image Correlation estimates", Optical Engineering, **27(10)**, pp.870-877.

Tippur H.V., Krishnaswamy S. and Rosakis A.J., 1991, "Crack tip deformation measurements using coherent gradient sensing", 2nd Int. Conf. on Photomechanics and Speckle Metrology, Proc. SPIEE **1554A**, pp 176-191.

Vendroux G., Knauss W.G., 1994a, "Deformation Measurements at the Sub-Micron Size Scale:I. Design of a Digital Scanning Tunneling Microscope", GALCIT report SM94-4, California Institute of Technology. Submitted to the Journal of Applied Mechanics with this paper.

Vendroux G., Knauss W.G., 1994b, "Deformation Measurements at the Sub-Micron Size Scale:III. Deformation Mechanisms in a Structural Polymer", GALCIT report SM94-6, California Institute of Technology. Submitted to the Journal of Applied Mechanics with this paper.

Vendroux G., 1994c, "Scanning Tunneling Microscopy in Micromechanics Investigations", Doctoral Thesis, GALCIT report SM93-36, California Institute of Technology.

DIC Scheme	Exact Least Square	Cross Correlation	Approx. Least Square	3-D Approx. Least Square
$s(\sqrt{u^2+v^2})$ $(pixel)$	7.78×10^{-3}	7.77×10^{-3}	7.78×10^{-3}	7.80×10^{-3}
$s(\gamma_{xx})$ $(pix./pix.)$	7.75×10^{-4}	7.66×10^{-4}	7.75×10^{-4}	7.61×10^{-4}
$s(\gamma_{yy})$ $(pix./pix.)$	7.04×10^{-4}	7.03×10^{-4}	7.04×10^{-4}	7.02×10^{-4}
$s(\gamma_{xy})$ $(pix./pix.)$	6.50×10^{-4}	6.46×10^{-4}	6.50×10^{-4}	6.44×10^{-4}
$\overline{\theta}$ $(Degree)$	1.64×10^{-2}	1.64×10^{-2}	1.64×10^{-2}	1.64×10^{-2}
$s(\theta)$ $(Degree)$	3.26×10^{-2}	3.26×10^{-2}	3.26×10^{-2}	3.26×10^{-2}
Run Time $(seconds)$	346.1	386.8	309.7	321.3

Table 1 Comparative results for the DIC codes.

DIC scheme	$R(pixel)$
Exact Least Square	1
Cross Correlation	1
Approx. Least Square	7
3-D Approx. Least Square	7

Table 2 Radius of convergence for the different DIC codes.

# of tests (DIC Runs)	$\overline{s(u)}$ $(pixel)$	$\overline{s(v)}$ $(pixel)$	$\overline{s(w)}$ (LSB)
75	0.08	0.08	90

Table 3: Standard Deviations of the Displacement Components for Translation tests.

List of Figures

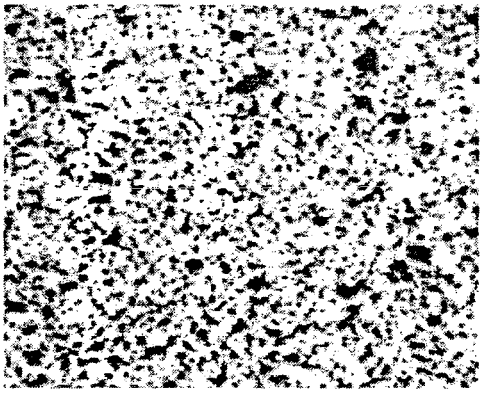

FIGURE 1 Typical speckle pattern.

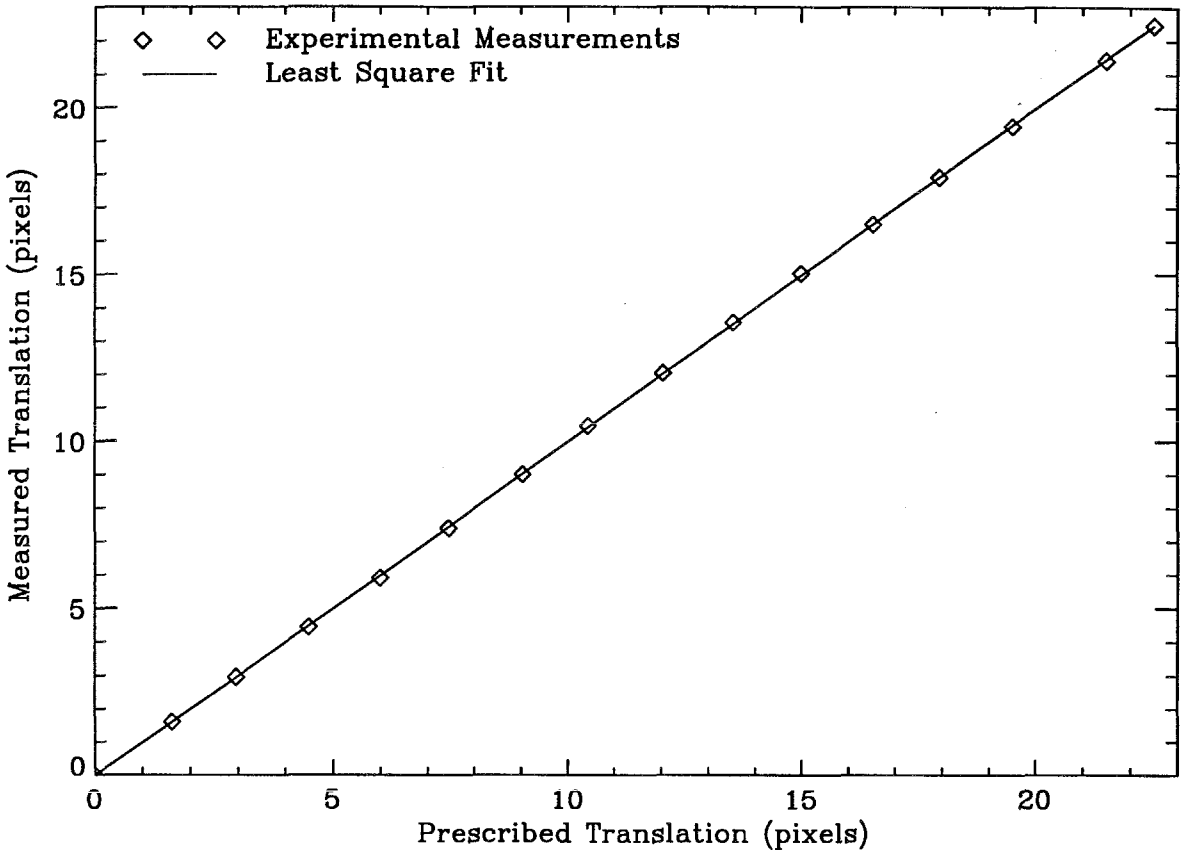

FIGURE 2 Comparison between the prescribed translation of a PVC specimen and the translation measured by Digital Image Correlation.

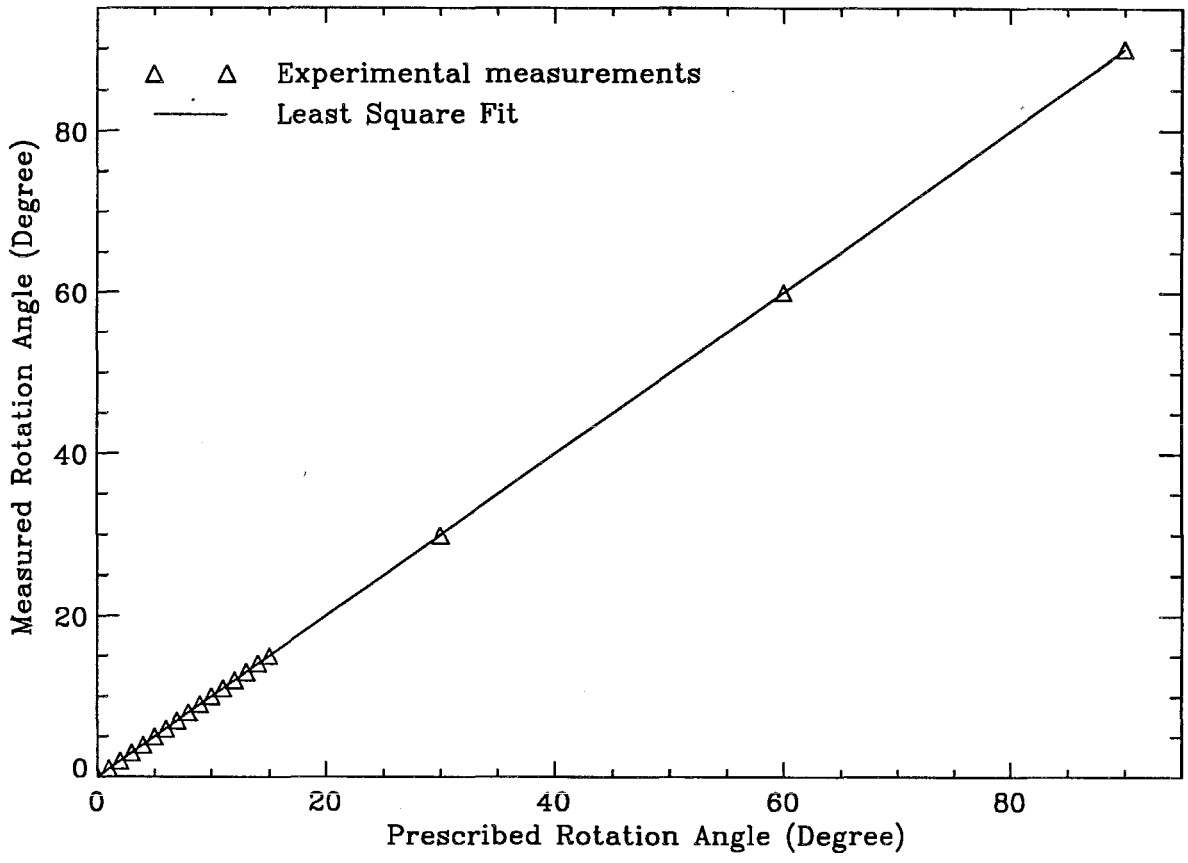

FIGURE 3 Comparison between the prescribed rotation of a PVC specimen and the rotation measured by the modified Digital Image Correlation.

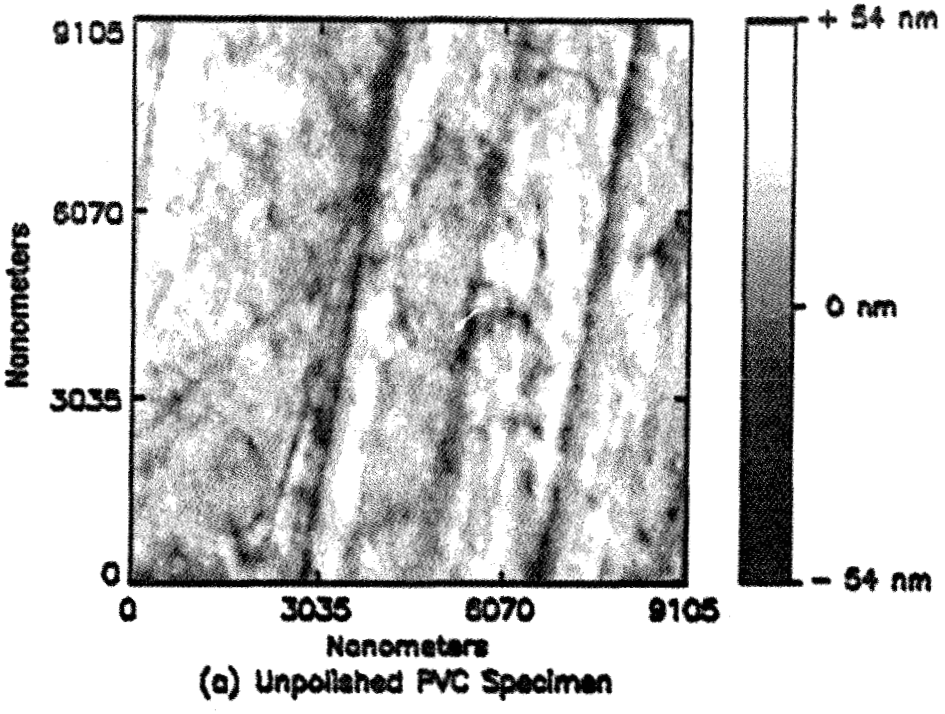

FIGURE 4 Typical topography of a PVC specimen surface.

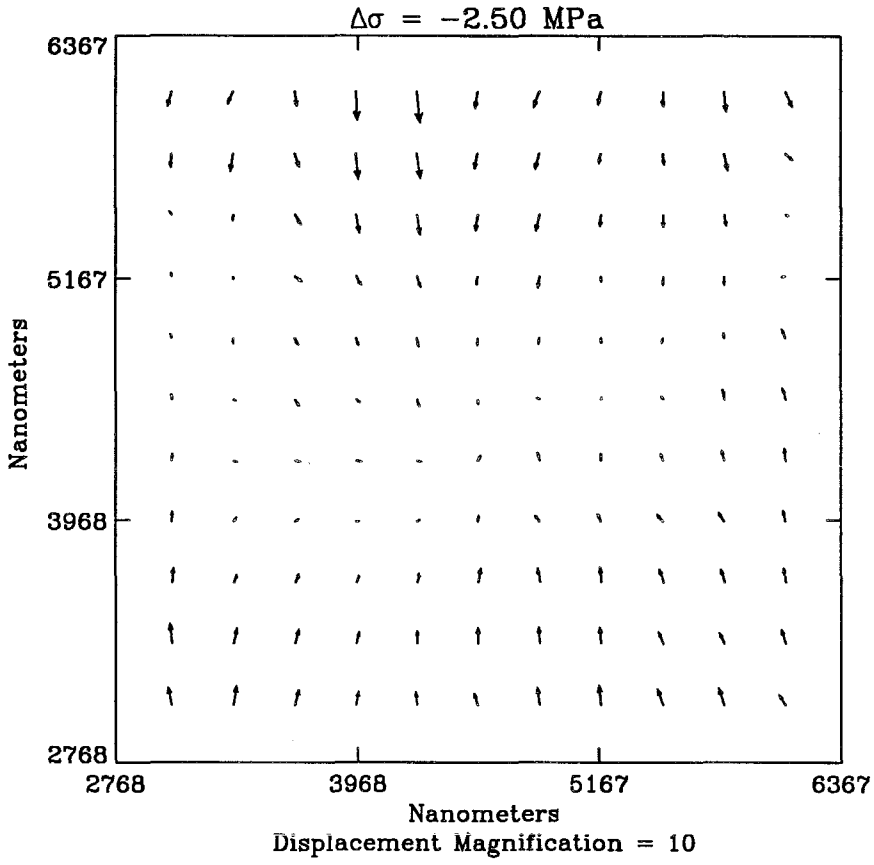

FIGURE 5 Measured displacement field of a PVC specimen upon unloading. The size of the displacement vector has been magnified by a factor of 10 with respect to the X and Y axes scale.

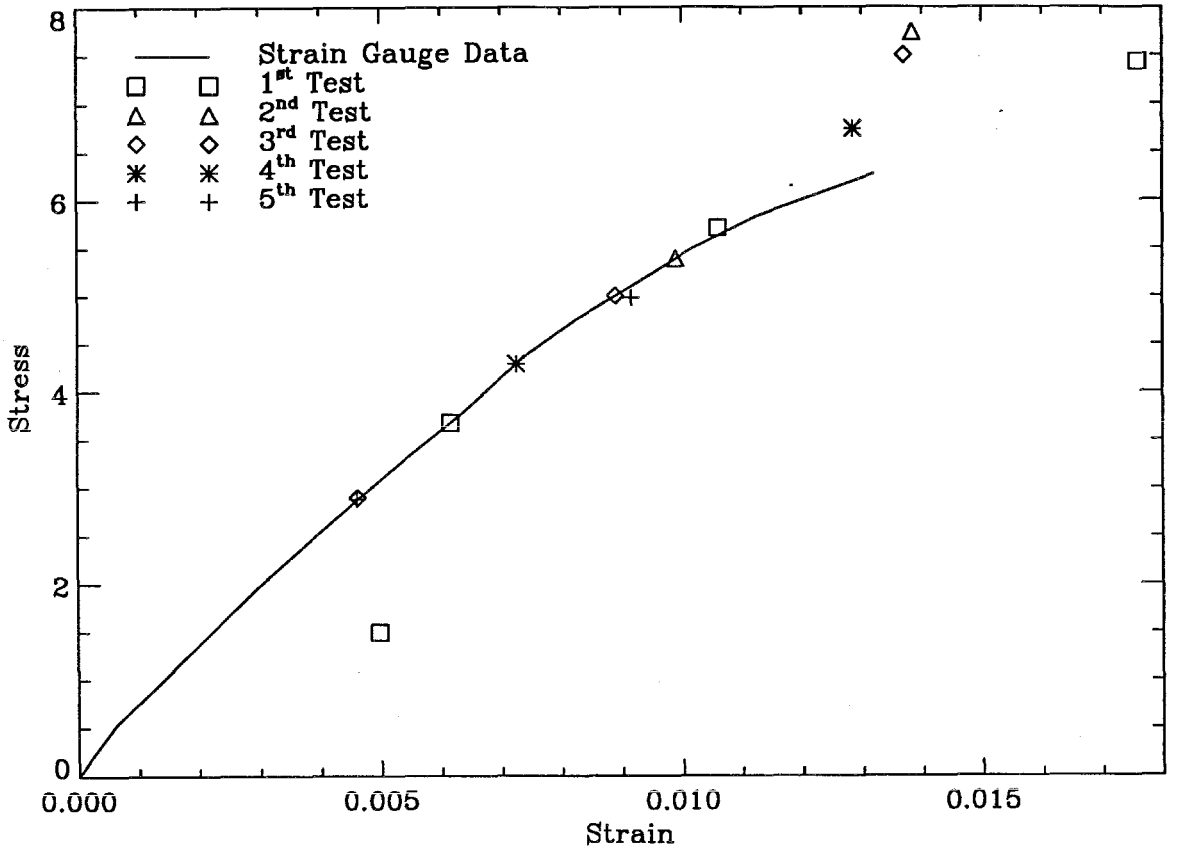

FIGURE 6 STM strain measurements compared to strain gauges results.